Comparative simulations of Taylor flow with surfactants based on sharp- and diffuse-interface methods

Sebastian Aland, Andreas Hahn, Christian Kahle, and Robert Nürnberg

Abstract We present a quantitative comparison of simulations based on diffuse- and sharp-interface models for two-phase flows with soluble surfactants. The test scenario involves a single Taylor bubble in a counter-current flow. The bubble assumes a stationary position as liquid inflow and gravity effects cancel each other out, which makes the scenario amenable to high resolution experimental imaging. We compare the accuracy and efficiency of the different numerical models and four different implementations in total.

1 Introduction

Taylor bubbles are long bubbles of gas in capillary tubes filled with a liquid. Nowadays, Taylor bubbles play a role in many technical applications, for example, in monolith structures that can be found in catalytic converters [52], multiphase monolith reactors [50, 42], or microfluidic channels [31, 47]. As these applications typically require bubbles of identical size, shape and distance to each other, the correct prediction of bubble hydrodynamics is of great value. Numerical simulations aim in

S. Aland
Institute of Scientific Computing, TU Dresden, 01062 Dresden and Faculty of Informatics/Mathematics, HTW Dresden, 01069 Dresden, e-mail: sebastian.aland@tu-dresden.de

A. Hahn
Institute for Analysis and Numerics, Otto-von-Guericke University Magdeburg, 39106 Magdeburg, Germany, e-mail: Andreas.Hahn@ovgu.de

C. Kahle
Chair of Optimal Control, Center for Mathematical Sciences, Technical University Munich, Boltzmannstraße 3, 85748 Garching, e-mail: christian.kahle@ma.tum.de

R. Nürnberg
Department of Mathematics, Imperial College London, London SW7 2AZ, UK e-mail: robert.nurnberg@imperial.ac.uk

this direction and provide a means to quantitatively compute the bubble dynamics and hence to optimize the desired flow properties on a computer.

Analysis of bubble speed has shown particular dependence on the thickness of the liquid film that occurs between the bubble and the capillary wall. Using lubrication approximation theory, Bretherton [22] was the first to give an analytical relation between film thickness and bubble speed. Contrary to the expectation, his result underestimated the film thickness for low capillary numbers, where it should be precise [11]. Explaining the discrepancy by means of viscosity, inertia, intermolecular forces or surface roughness failed. However, impurities of surface active agents (surfactants) are known to affect the film thickness, as surfactants soften the interface and induce additional Marangoni forces. In [49] Bretherton's theory was extended to a case with trace amounts of surfactants present. They showed that the film thickness could increase by a maximum factor of $4^{\frac{2}{3}}$, which could explain the discrepancy of Bretherton's results.

These observations show that the inclusion of surfactant dynamics is crucial for the correct prediction of Taylor flow. However, numerical simulations of Taylor flow with surfactants appeared only recently [33, 48], due to the complicated interplay of hydrodynamics, surface evolution and surfactant dynamics. In [33] the effect of surfactant on the terminal velocity of a rising Taylor bubble in a vertical pipe was studied using an interface tracking method. In [48] the effect of surfactant on the motion of a Taylor bubble moving through a capillary tube was investigated numerically using a finite-difference front tracking method.

The rigorous assessment of simulation accuracy, requires benchmarking, i.e., a quantitative code-to-code comparison with physically relevant physical parameters and practically relevant output parameters. In [8] it is stressed that Taylor flow poses a perfect two-phase flow problem for benchmarking, due to its sensitivity to a wide range of surface tensions, and since it admits non-trivial stationary solutions that are amenable to high quality experimental imaging. Aland et al. [6] and later Marschall et al. [45] have already presented such benchmark studies for Taylor flow without surfactants, and both provided highly accurate reference data in two and three dimensions, as well as comparison to experiments.

The goal of this chapter is to extend the work of [6] to include soluble surfactants, and hence to provide the first benchmark study of two-phase flow with surfactants. Therefore we simulate a single Taylor bubble in a counter-current flow scenario, where the bubble assumes a stationary state as buoyancy and liquid inflow balance each other. We examine the effect of surfactant amount, surfactant elasticity and Peclet number on bubble shape, speed and film thickness. Moreover, we analyze surfactant profiles along the surface and in the liquid bulk. Four independent numerical codes are compared, two based on a sharp-interface model, and two based on a diffuse-interface model.

The structure of the chapter is as follows. In Sec. 2 we present the employed sharp- and diffuse-interface models. The hydrodynamic part of the benchmark problem is summarized in Sec. 3, including an overview of the results from [6]. Finally, in Sec. 4, we present the new results including surfactants and assess the accuracy and efficiency of the numerical codes.

2 Mathematical models

In this section, the mathematical models for the diffuse- and the sharp-interface models are given.

2.1 Sharp interface model

The sharp-interface model consists of the Navier–Stokes equations, a convection-diffusion equation in the bulk and a convection-diffusion equation on the interface.

The domain Ω consists of the two phases, where $\Omega_1(t)$ is the inner phase and $\Omega_2(t)$ the outer phase. The phases are immiscible, i.e. $\Omega_1(t) \cap \Omega_2(t) = \emptyset$, and they are separated by the interface $\Gamma(t) = \overline{\Omega}_1(t) \cap \overline{\Omega}_2(t)$. The Navier–Stokes equations in the time interval $(0,T]$ are

$$\nu\left(\frac{\partial \mathbf{u}}{\partial t} + (\mathbf{u}\cdot\nabla)\,\mathbf{u}\right) - \nabla\cdot\mathbb{S}(\mathbf{u},p) = \mathrm{Fr}^{-1}\nu\mathbf{g},\ \ \nabla\cdot\mathbf{u} = 0 \quad \text{in } \Omega_i(t),\ i=1,2, \tag{1}$$

where $\mathbf{u}$ is the velocity and p is the pressure field, Fr is the Froude number, $\mathbf{g} = (0,-1)^T$ is the gravity vector and ν the dimensionless density. The dimensionless stress tensor $\mathbb{S}$ is given by

$$\mathbb{S}(\mathbf{u},p) = \mathrm{Re}^{-1}\left(\nabla\mathbf{u} + (\nabla\mathbf{u})^T\right) - p\mathbb{I}. \tag{2}$$

The dimensionless density ν and the Reynolds number Re are piecewise constant with respect to the phases,

$$\mathrm{Re} = \begin{cases} Re_2\eta_2/\eta_1 & \text{, in } \Omega_1 \\ Re_2 & \text{, in } \Omega_2 \end{cases},\ \nu = \begin{cases} \rho_1/\rho_2 & \text{, in } \Omega_1 \\ 1 & \text{, in } \Omega_2 \end{cases},\ Re_2 = \frac{\rho_2 V d}{\eta_2},\ Fr = \frac{V^2}{gd}, \tag{3}$$

where V is the characteristic velocity, d is the characteristic length, η_i is the dynamic viscosity of phase i, ρ_i is the density of phase i, and g is the gravitational acceleration.

On the interface the following matching conditions are specified. The surface tension force balances the jump in the stress tensor,

$$[|\mathbb{S}(\mathbf{u},p)|]\cdot\mathbf{n}_\Gamma = \nabla_\Gamma\cdot(\sigma\mathbb{P}_\Gamma) \quad \text{on } \Gamma(t), \tag{4}$$

where $[|f|] = f|_{\Omega_1} - f|_{\Omega_2}$ denotes the jump over Γ, $\mathbf{n}_\Gamma$ is the unit normal on Γ, pointing into Ω_2, $\nabla_\Gamma\cdot$ is the surface divergence on Γ, $\sigma = \sigma(c_\Gamma)$ is the nondimensional surface tension which is dependent on the surface surfactant concentration c_Γ, and $\mathbb{P}_\Gamma = \mathbb{I} - \mathbf{n}_\Gamma\otimes\mathbf{n}_\Gamma$ denotes the projection onto the tangential space of Γ. The continuity condition for the velocity $\mathbf{u}$ and the interface velocity $\mathbf{w}$ are

$$[|\mathbf{u}|] = 0, \quad \mathbf{w}\cdot\mathbf{n}_\Gamma = \mathbf{u}\cdot\mathbf{n}_\Gamma \quad \text{on } \Gamma(t). \tag{5}$$

The Langmuir law for the surface tension coefficient reads

$$\sigma(c_\Gamma) = \mathrm{We}^{-1}(1 + \mathrm{E}\ln(1 - c_\Gamma)), \tag{6}$$

where $\mathrm{We} = \rho_2 V^2 d\sigma_0^{-1}$ is the Weber number and $\mathrm{E} = RT_\infty c_\Gamma^\infty \sigma_0^{-1}$ is the surface elasticity, with the universal gas constant R, the equilibrium temperature T_∞, the maximum packing surface surfactant concentration c_Γ^∞, and the surface tension coefficient σ_0.

The surfactant transport in the bulk and on the surface is modelled by convection-diffusion-reaction equations. The surfactant is considered to be soluble into the liquid phase Ω_2 only,

$$\frac{\partial c}{\partial t} + \mathbf{u} \cdot \nabla c = \mathrm{Pe}^{-1} \Delta c \qquad \text{in } \Omega_2(t), \tag{7}$$

$$\mathrm{Pe}^{-1} \mathbf{n}_\Gamma \cdot \nabla c = -S(c, c_\Gamma) \qquad \text{on } \Gamma(t), \tag{8}$$

$$\dot{c}_\Gamma + c_\Gamma \nabla_\Gamma \cdot \mathbf{u} = \mathrm{Pe}_\Gamma^{-1} \Delta_\Gamma c_\Gamma + S(c, c_\Gamma) \qquad \text{on } \Gamma(t), \tag{9}$$

where c is the bulk surfactant concentration, $\dot{c}_\Gamma$ denotes the material derivative of c_Γ and $\Delta_\Gamma = \nabla_\Gamma \cdot \nabla_\Gamma$ denotes the Laplace–Beltrami operator on Γ. In addition, $\mathrm{Pe} = VdD^{-1}$ and $\mathrm{Pe}_\Gamma = VdD_\Gamma^{-1}$ denote the Peclet number in the bulk and on the surface, with D and D_Γ the diffusion coefficients in the bulk and on the surface, respectively. The ad- and desorption term S is given according to the Langmuir sorption law,

$$S(c, c_\Gamma) = \mathrm{Da}\, c\,(1 - c_\Gamma) - \mathrm{Bi}\, c_\Gamma, \tag{10}$$

where $\mathrm{Da} = k_a c_\Gamma^\infty V^{-1}$ and $\mathrm{Bi} = k_d d V^{-1}$ are the Damköhler and the Biot number, respectively, with adsorption coefficient k_a and the desorption coefficient k_d.

2.2 Diffuse-interface model

In addition to the above description of the interface as a sharp hyper-surface, so-called diffuse-interface models can be used. Diffuse-interface models account for a partial mixing of the fluids at a small length scale. Therefore the interface is represented as a thin layer of finite thickness ε. An auxiliary phase-field function ϕ is used to indicate the phases. The phase-field function varies smoothly between distinct values in both phases, here $\phi = 1$ in the gas phase Ω_1 and and $\phi = -1$ in the liquid phase Ω_2. The interface can be associated with an intermediate level set of the phase-field function (here $\phi = 0$). For a comprehensive overview on diffuse-interface models, we refer to another chapter of this book [5].

The simplest diffuse-interface model consists of the following coupled Navier–Stokes Cahn–Hilliard equations defined in $\Omega \times (0, T]$:

$$\nu(\phi)\left(\frac{\partial \mathbf{u}}{\partial t}+\mathbf{u}\cdot\nabla\mathbf{u}\right)+\nabla p-\nabla\cdot\left(\mathrm{Re}(\phi)^{-1}\left(\nabla\mathbf{u}+\nabla\mathbf{u}^T\right)\right)$$
$$=\mathrm{Fr}^{-1}\nu\mathbf{g}+\sigma\mu\nabla\phi+\frac{1}{2}|\nabla\phi|\mathbb{P}_\Gamma\nabla\sigma, \tag{11a}$$
$$\nabla\cdot\mathbf{u}=0, \tag{11b}$$
$$\frac{\partial\phi}{\partial t}+\mathbf{u}\cdot\nabla\phi=\nabla\cdot(M(\phi)\nabla\mu), \tag{11c}$$
$$\mu=\tfrac{3}{2\sqrt{2}}\left(\varepsilon^{-1}W'(\phi)-\varepsilon\Delta\phi\right). \tag{11d}$$

Here μ is the chemical potential, M a mobility function, the function $W(\phi)=\frac{1}{4}(\phi^2-1)^2$ is a double-well potential and the surface projection $\mathbb{P}_\Gamma=\mathbb{I}-\mathbf{n}_\phi\otimes\mathbf{n}_\phi$ here involves the diffuse-interface normal $\mathbf{n}_\phi=\nabla\phi/|\nabla\phi|$. The Reynolds number and nondimensional density are defined as linear interpolations,

$$\mathrm{Re}(\phi)=\frac{1+\phi}{2}\mathrm{Re}_2\frac{\eta_2}{\eta_1}+\frac{1-\phi}{2}\mathrm{Re}_2,\quad \nu(\phi)=\frac{1+\phi}{2}\frac{\rho_1}{\rho_2}+\frac{1-\phi}{2}.$$

The surfactant transport equations in the bulk and on the surface are extended to the whole domain Ω by the diffuse-domain approach, see also [5]. The resulting equations in $\Omega\times(0,T]$ are

$$\frac{\partial}{\partial t}(\chi(\phi)c)+\mathbf{u}\cdot\nabla(\chi(\phi)c)=\mathrm{Pe}^{-1}\nabla\cdot(\chi(\phi)\nabla c)-\delta(\phi)S(c,c_\Gamma), \tag{12}$$
$$\frac{\partial}{\partial t}(\delta(\phi)c_\Gamma)+\mathbf{u}\cdot\nabla(\delta(\phi)c_\Gamma)=\mathrm{Pe}_\Gamma^{-1}\nabla\cdot(\delta(\phi)\nabla c_\Gamma)+\delta(\phi)S(c,c_\Gamma), \tag{13}$$

where $\delta(\phi)=|\nabla\phi|/2$ and $\chi(\phi)=(1-\phi)/2$ are approximations to the surface Dirac delta function and the characteristic function of the liquid domain, respectively.

As an alternative, we also consider the following diffuse-interface model, where we replace (11) by an extension of the thermodynamically consistent model from [1] that additionally incorporates surfactants, see also [29, 2]. The model is given by

$$\frac{\partial}{\partial t}(\nu\mathbf{u})+\left(\left(\nu\mathbf{u}-\frac{\rho_2-\rho_1}{2\rho_2}M(\phi)\nabla\mu\right)\cdot\nabla\right)\mathbf{u}+\nabla p-\nabla\cdot\left(\mathrm{Re}^{-1}(\nabla\mathbf{u}+\nabla\mathbf{u}^T)\right)$$
$$=\mu\nabla\phi+\delta(\phi)\nabla\sigma+\mathrm{Fr}^{-1}\nu\mathbf{g}-\chi'(\phi)\left(G(c)-G'(c)c\right)\nabla\phi, \tag{14a}$$
$$\nabla\cdot\mathbf{u}=0, \tag{14b}$$
$$\frac{\partial\phi}{\partial t}+\mathbf{u}\cdot\nabla\phi=\nabla\cdot(M(\phi)\nabla\mu), \tag{14c}$$
$$\mu+\nabla\cdot\left(\tfrac{2}{\pi}\varepsilon\sigma\nabla\phi\right)=\tfrac{2}{\pi}\varepsilon^{-1}\sigma W'(\phi)+\chi'(\phi)\left(G(c)-G'(c)c\right), \tag{14d}$$

where we note that $\chi'(\phi)=-\frac{1}{2}$. Here all variables and parameters are defined as before, except for the diffuse delta function, which is now

$$\delta(\phi) = \frac{2}{\pi}\left(\frac{\varepsilon}{2}|\nabla\phi|^2 + \frac{1}{\varepsilon}W(\phi)\right),$$

and for the double-well potential W, which in our model is given by the double-obstacle potential

$$W(\phi) = \begin{cases} \frac{1}{2}(1-\phi^2) & \text{if } |\phi| \leq 1, \\ +\infty & \text{else.} \end{cases}$$

In particular, (14d) abbreviates a variational inequality in this setting. The energy density $G(c)$ depends on the chosen sorption model, see [29], and in the case of the Langmuir sorption law (6) it holds that $G(c) - G'(c)c = -\mathrm{We}^{-1}\mathrm{E}\,c$.

3 Benchmark without surfactants

First, we consider the hydrodynamics of a clean surface without surfactants. In this case, the equations for c_Γ and c are dropped and the surface tension assumes the constant value $\sigma = \mathrm{We}^{-1}$. A first benchmark for two dimensional and axisymmetric Taylor flow hydrodynamics was presented in [6]. In this section, we recall the benchmark setting and results of [6], before we use the same setting and parameters to include surfactants in Sec. 4.

3.1 Setting and parameters

We consider a single bubble in a two-dimensional channel. The initial bubble shape is prescribed as two half-circles connected by straight edges, the computational domain is $\Omega = [0,1] \times [0,10]$, see Fig. 1. Flow is created by imposing a pressure gradient between the channel inlet and outlet. A co-moving grid is employed such that the bubble remains in the center of the computational domain and evolves to a quasi-stationary state.

The hydrodynamic parameters are chosen from realistic Taylor flow experiments, see Tab. 1. The problem is essentially described by three different nondimensional numbers, the Reynolds number, the Weber number and the capillary number, only two of which are independent, see Tab. 2.

3.2 Benchmark results

For the benchmark problems without surfactant three different scenarios where chosen [6], namely a 2D Taylor flow, the Bretherton problem, with varying capillary numbers, a 3D Taylor flow under the assumption of rotational symmetry, with vary-

ρ_L	$1{\cdot}10^{3}$	$\frac{\mathrm{kg}}{\mathrm{m}^3}$	density of liquid phase
ρ_G	$1{\cdot}10^{-3}$	ρ_L	density of gas phase
η_L	$1{\cdot}10^{-2}$	Pa s	dynamic viscosity of liquid phase
η_G	$1{\cdot}10^{-3}$	η_L	dynamic viscosity of gas phase
σ_0	$5{\cdot}10^{-4}$	$\frac{\mathrm{N}}{\mathrm{m}}$	surface tension coefficient
V	$1{\cdot}10^{-3}$	$\frac{m}{s}$	characteristic velocity
d	$1{\cdot}10^{-3}$	m	characteristic length, width of computational domain
L	$1{\cdot}10^{-2}$	m	length of computational domain

Table 1 Physical parameters for the numerical benchmark.

Re_2	$\frac{\rho_L V d}{\eta_L}$	0.1	Reynolds no. in liquid phase
Ca	$\frac{\eta_L V}{\sigma_0}$	$2 \cdot 10^{\{-4,-3,-2,-1\}}$	capillary no.
We	$Re_2\, Ca$	$0.1 \cdot Ca$	Weber no.

Table 2 Dimensionless quantities for the numerical benchmark.

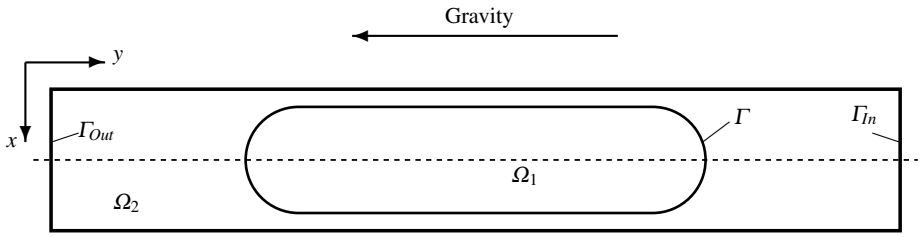

Fig. 1 Initial bubble setting and boundaries.

ing capillary numbers, and a single 3D rotational symmetric Taylor bubble which was compared to experimental data. Note that rotational symmetry of the bubble can then be safely assumed due to the high surface tension.

Participating numerical codes were based both on a classical sharp-interface approach and also on a diffuse-interface model. For the sharp-interface model, two numerical codes using Arbitrary Lagrangian Eulerian (ALE) coordinates and a moving mesh were employed and for the diffuse-interface approach two different but similar mathematical models were compared. Data from all codes were compared to each other for varying capillary numbers in terms of velocity profiles, bubble shapes and pressure distribution.

By using a high-energy synchrotron radiation source [21], very precise measurements of the bubble shape were obtained. The different mathematical models and numerical codes obtained very good agreement to each other. The difference of the simulated bubble shapes to the experimental data was somewhat higher. While the exact reason for this slight disagreement is unclear as of yet, measurement errors in the experiment could explain part of this problem.

The width of the liquid film between the bubble and the capillary wall is one of the most sensible markers for Taylor flow. In a two-dimensional theoretical investigation, a relation between the capillary number and the film width has been derived [22]. For small capillary numbers ($\mathrm{Ca} \leq 3 \cdot 10^{-3}$) it was found that

$$h_{\text{film}} = 0.669\, d\, \mathrm{Ca}^{2/3},$$

where d denotes the diameter of the 2D channel. For larger capillary numbers ($0.05 \leq \mathrm{Ca} \leq 100$) numerical simulations with the boundary element method led to the approximation [32]

$$h_{\text{film}} = 0.209\, d \left(1 - \exp(-1.69 \cdot \mathrm{Ca}^{0.5025})\right).$$

Both formulas have been validated in the benchmark [6] for a range of capillary numbers $10^{-4} \leq \mathrm{Ca} \leq 1$. For high capillary numbers, all models showed perfect agreement with the film thickness approximations. For lower capillary numbers, the film width becomes very small and hard to resolve with the diffuse-interface models, because it requires a computationally expensive small interface thickness. For this reason only few results are shown in [6] for small Ca using diffuse-interface models.

In summary, in [6] it is concluded that despite their conceptual differences, the tested sharp- and diffuse-interface codes are well-applicable for the physically relevant parameter regime. Only diffuse-interface methods are restricted to ranges of moderately large capillary numbers to resolve the corresponding small film thickness and provide highly accurate results.

4 Benchmark with surfactant

In the following we present an extension of the benchmark presented in the previous section to also include soluble surfactants. The basic setup and all hydrodynamic parameters are left unchanged. The additional parameters and conditions for the surfactants are stated below.

4.1 Setup

The benchmark setting is designed to simulate a single Taylor bubble in a vertical channel in a counter flow. As discussed earlier, stationary states are advantageous in particular for later comparison with experiments. Such a stationary equilibrium can be reached when buoyancy (upwards) and counter-flow (downwards) balance each other and the net velocity of the Taylor bubble becomes zero. To this end, the inflow velocity is adjusted during the time evolution towards the equilibrium state,

see Sec. 4.1.2. Simultaneously, this ensures that the bubble remains in the center of the computational domain.

4.1.1 Initial conditions

The initial bubble diameter is set to 0.7 units, the total bubble length is set to 4.7 units. The initial fluid is at rest, i.e. $\mathbf{u}(0) = 0$ in Ω. The initial surfactant concentration in the bulk is homogeneous $c(0) = c_0$. The initially constant surface surfactant concentration is chosen according to the equilibrium condition

$$\frac{\mathrm{Da}}{\mathrm{Bi}} = \frac{c_\Gamma}{c(1-c_\Gamma)}. \tag{15}$$

4.1.2 Boundary conditions

On the inflow boundary Γ_{In} the fluid velocity is prescribed by the following Dirichlet boundary condition

$$\mathbf{u}|_{\Gamma_{In}}(x,y,t) = -4u_{max}(t)x(1-x)\mathbf{e}_y \quad x \in [0,1], \tag{16}$$

where u_{max} is the maximum inflow velocity, and $\mathbf{e}_y$ denotes the unit vector in y-direction. The value of u_{max} is updated in every time step to reach a stationary bubble position according to the following law:

$$u_{max}^{n+1} = u_{max}^n + u_{bubble}^n, \tag{17}$$

where superscripts indicate time step indices and u_{bubble} is the bubble speed in the longitudinal direction, i.e. in the y-direction. We also set $u_{max}^0 = 0$.

The inflowing liquid contains a constant surfactant concentration, which leads to the Dirichlet boundary condition

$$c|_{\Gamma_{In}} = c_0. \tag{18}$$

On the outflow boundary Γ_{Out} a do-nothing (stress free) condition is given for the fluid velocity and the surfactant concentration, i.e.

$$\mathbf{n} \cdot \mathbb{S}(\mathbf{u}, p)|_{\Gamma_{Out}} = 0, \qquad \mathbf{n} \cdot \nabla c|_{\Gamma_{Out}} = 0, \tag{19}$$

where $\mathbf{n}$ denotes the outer unit normal on $\partial\Omega$. At the capillary wall a no-slip condition for the fluid is assumed

$$\mathbf{u}|_{\Gamma_W} = 0. \tag{20}$$

The flux of surfactant is obstructed by the capillary wall, hence, together with the no-slip condition for the fluid, a homogeneous Neumann condition is needed for the

surfactant

$$\mathbf{n} \cdot \nabla c|_{\Gamma_W} = 0. \tag{21}$$

4.2 Surfactant-related parameters

Due to the wide variety of different surfactants with different properties, we freely choose the surfactant-related parameters. We use the fixed Damköhler and Biot numbers $\mathrm{Da} = \mathrm{Bi} = 0.01$. The other surfactant-related parameters are varied as follows. The surface elasticity $\mathrm{E} \in \{0.5, 1.0\}$, the initial surfactant concentration $c_0 \in \{0.02, 0.08\}$ and the surface and bulk Peclet numbers are chosen to be equal $\mathrm{Pe} = \mathrm{Pe}_\Gamma \in \{1, 10\}$. The end time is specified as $T = 10$. The remaining parameters are: $\mathrm{Re} = 0.1$, $\mathrm{We} = 2 \cdot 10^{-3}$ and $\mathrm{Fr} = 1 \cdot 10^{-4}$.

4.3 Numerical methods

Four different solvers using different numerical approaches to the capillary problem at hand were used. In the following we give a short description of each solver.

4.3.1 Solvers implementing the sharp-interface model

The two sharp-interface solvers BGN and MooNMD use the Finite Element Method (FEM) to implement the sharp-interface model.

BGN

The solver BGN, realized within the finite element toolbox ALBERTA [51], is based on an implementation of the parametric finite element approximation introduced in [17]. In particular, it is based on an unfitted finite element method for two-phase flow [14, 19], where the bulk mesh, on which velocity, pressure and bulk surfactant are approximated, is totally independent of the polygonal interface mesh, on which the curvature and the surface surfactant are approximated.

In the bulk phase, the solver uses a standard P_2-P_1 Taylor–Hood element with a simple XFEM enrichment of the pressure space. In order to better capture the details around the phase interface, the bulk mesh is adapted to yield a fine resolution close to the interface, and a coarser resolution further away from it. As the bulk mesh is not fitted to the discrete interface, standard refinement and coarsening algorithms can be used to achieve the desired adaptation. In addition, an implicit tangential motion of the interface nodes leads to a nearly equidistributed discrete interface

throughout [14]. As a consequence, no remeshings of interface or bulk meshes are needed in any of the computations.

An implicit Euler time stepping scheme, leading to linear subproblems to be solved at each time step, is employed. In the absence of surfactants, the time stepping scheme can be shown to be unconditionally stable [19]. The stability crucially relies on a variational treatment of curvature, and an appropriate coupling between bulk and interface approximations. The coupled linear systems arising at each time level are solved with the help of a Schur complement approach, which reduces the system to a standard saddle point problem arising from discretizations of Navier–Stokes problems. These saddle point problems are solved with a preconditioned GMRES iterative solver. More details on the solution procedure can be found in [19]. Finally, for the computations in this paper the symmetry of the planar problem was exploited. In particular, only half of the domain was used as the computational domain.

Variants of the BGN package have been successfully applied to dendritic growth [12], snow crystal growth [13], two-phase incompressible Navier–Stokes flow [14, 19], featuring insoluble [16] and soluble [17] surfactants, as well as to two-phase flow with a Boussinesq–Scriven surface fluid [18] and to the dynamics of fluidic membranes and vesicles [15, 20].

MooNMD

The MooNMD solver used here is branch based on the general purpose finite element solver MooNMD [39]. This package has been successfully applied, e.g. in the solution of the steady state and time dependent incompressible Navier–Stokes equations [37, 36, 38], large eddy simulations [35], free boundary value problems with capillary surfaces and ferrofluids [43, 30], multiphase problems with and without surface active agents [34, 25, 26], population balance systems [40, 27, 41] and convection-diffusion equations by stabilized finite elements [3, 46].

The MooNMD solver used here employes a Arbitrary Lagrangian Eulerian (ALE) finite element method [23, 24], such that the grid is always aligned to the interface and no cut-cells exist. The time discretization is done with a semi-implicit Euler scheme, that decouples the system (1) and (7) and allows for an iterative solution for each component.

A modified P_2-P_1 Taylor Hood finite element space is used for the Navier–Stokes equations, that allows pressure jump across the interface, but is continuous in the bulk phases.

For the surfactant a P_2 finite element space is used, in the bulk and on the surface as well.

The interface approximation is of second order, consisting of piecewise quadratic elements. Thus, the Navier–Stokes equation, the bulk transport and the surface transport equation are solved on a second order isoparametric grid at the interface. Further, the axisymmetry of the problem is employed and the computation is done only

on one half of the domain using appropriate boundary conditions at the symmetry axis.

4.3.2 Solvers implementing the phase-field model

The two diffuse-interface solvers AMDiS and 2PStab were used for this study.

AMDiS

AMDiS is an adaptive finite element toolbox which is designed for fast implementation of arbitrary PDEs. The software has been already been used for benchmarks of two-phase flow [10, 4, 6]. Extensions for interfacial molecules[44], nanoparticles[9] and lipid bilayer membranes [7, 44] have been implemented.

The simple diffuse-interface model from (11)-(13) is used. A semi-implicit Euler time stepping algorithm is employed together with space discretization by a Taylor–Hood element for the Navier–Stokes equation, with P_1-elements for p and P_2-elements for $\mathbf{u}$, ϕ, μ, c, c_Γ. The occurring linear systems are solved with the direct solver UMFPACK.

We use $\varepsilon = 0.0075$ and an adaptive grid with prescribed grid size $h = 1/128$ at the interface and $h = 1/32$ away from the interface. The mobility is kept constant at $M = 5 \cdot 10^{-5}$. Equidistant time steps of size 10^{-3} are used. Simulations until the end time $T = 10$ correspond to a computational time of $50h$.

2PStab

This code uses ideas from [28], where two-phase flow without surfactants is simulated, to obtain an energy stable time discretization for (14). Details will be provided elsewhere.

The code is written in C++ using the FEniCS package. The linear algebra backend is PETSc, and linear systems are solved using the direct solver MUMPS. The spatial discretization is represented using the library ALBERTA [51]. We use Taylor–Hood elements for the spatial discretization of the Navier–Stokes equation, i.e. P_2 elements for the velocity field $\mathbf{u}$ and P_1 elements for the pressure p. The further variables, i.e. ϕ, μ, c, c_Γ, are discretized using P_1 elements.

We set $\varepsilon = 0.02$ and $M(\phi) = 10^{-5}\left(1 - 0.99\phi^2\right)$, approximating a degenerate mobility. To resolve the interfacial region, i.e. $|\phi| < 1$, we use triangles with diameter $h = 0.004$, while in the bulk regions we use $h = 0.025$. The time step size is $\tau = 5 \cdot 10^{-5}$.

4.4 Results

Different benchmark values are considered. Apart from the numerical values c, c_Γ and u_{max}, calculated by the codes, some of them are determined by a post process. Due to the different nature of the methods used here, the post process can differ likewise.

Here, the film width h_{film} is defined as the minimal distance between bubble and wall. For the sharp-interface schemes, h_{film} is computed directly from the disrete interface representation, while the diffuse-interface schemes use the zero level contour line of ϕ.

The bulk surfactant mass m_c and surface surfactant mass m_{c_Γ} are defined as the total amount of surfactant present in the bulk and on the surface, respectively. In case of the sharp-interface schemes the bulk surfactant exist in Ω_2 and the surface surfactant exists on Γ. The corresponding masses are calculated as

$$m_c = \int_{\Omega_2} c, \quad m_{c_\Gamma} = \int_\Gamma c_\Gamma.$$

In the case of the diffuse-interface schemes, the quantities c and c_Γ are defined in the whole domain Ω and, thus the masses are calculated as

$$m_c = \int_\Omega \frac{1}{2}(1-\phi)c, \quad m_{c_\Gamma} = \int_\Omega \delta(\phi)c_\Gamma.$$

Having defined the benchmark values, we take a closer look at the results in the following.

Fig. 2 shows the time evolution of the maximum inflow velocity u_{max} for the simulation parameters $(c_0, Pe, Pe_\Gamma, E) = (0.02, 1, 1, 1)$, exemplarily. All four codes show a similar behavior, after some oscillations u_{max} reaches a stationary state already before $t = 1$. According to the adaption law for u_{max}, recall (17), this also implies the stationarity of the bubble position in the channel. The sharp-interface results are very close to each other and so are the diffuse-interface results, that both predict a slightly smaller bubble velocity.

In Tab. 3 the final counter current flow velocity is shown for all chosen parameter combinations. Note that the variation of the flow velocity across the different numerical models dominates the variation across different parameters. The missing values in Tab. 3, in particular for $c_0 = 0.08, Pe = Pe_\Gamma = 10$, are caused by numerical problems due to high surfactant concentration at the bubble rear and the corresponding low surface tensions.

Next we look at the evolution of surfactant concentrations. The bulk surfactant mass and the surface surfactant mass over time are shown in Figs. 3 and 4, respectively. The bulk surfactant mass decreases over time and reaches a stationary state. It can be seen that the surfactant mass equilibrates slower than the inflow velocity and the stationary state is not reached until approximately $t = 5$. Agreement among the codes is particularly high between AMDiS and MooNMD, despite the concep-

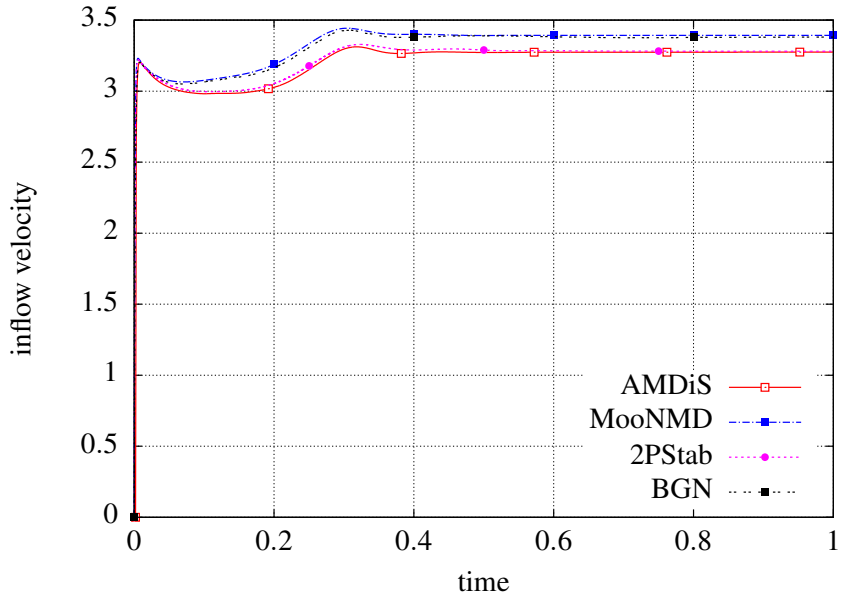

Fig. 2 Maximum inflow velocity over time (detail), for $(c_0, Pe, Pe_\Gamma, E) = (0.02, 1, 1, 1)$.

Table 3 Maximum counter flow velocity u_{max} at the stationary state for different simulation parameters.

$c_0 = 0.02$	$Pe = Pe_\Gamma = 1$		$Pe = Pe_\Gamma = 10$	
	$E = 0.5$	$E = 1$	$E = 0.5$	$E = 1$
AMDiS	3.27506	3.27336	3.27539	3.27391
MooNMD	3.39283	3.39284	3.39283	3.39284
2PStab ($t = 1$)	3.28185	3.28102	3.28248	3.28087
BGN	3.37914	3.37773	3.36149	3.35499
$c_0 = 0.08$	$Pe = Pe_\Gamma = 1$		$Pe = Pe_\Gamma = 10$	
	$E = 0.5$	$E = 1$	$E = 0.5$	$E = 1$
AMDiS	3.26413	3.25311	-	-
MooNMD	3.39286	3.38990	3.39198	3.39203
2PStab ($t = 1$)	3.29367	-	-	-
BGN	3.35935	3.33733	3.33063	3.31528

tual differences between sharp- and diffuse-interface models. Due to the small time steps used, the simulation of 2PStab is limited to the end time $t = 1$.

In Fig. 4 we depict the temporal evolution of the surface surfactant mass. We observe a slow decrease of the surface surfactant mass over time, indicating that a discrete stationary solution is not yet found at $T = 10$. Although the continuous problem would eventually lead to a stationary state, for which conservation of mass holds trivially, the loss of exact divergence free flow in the discrete setting may

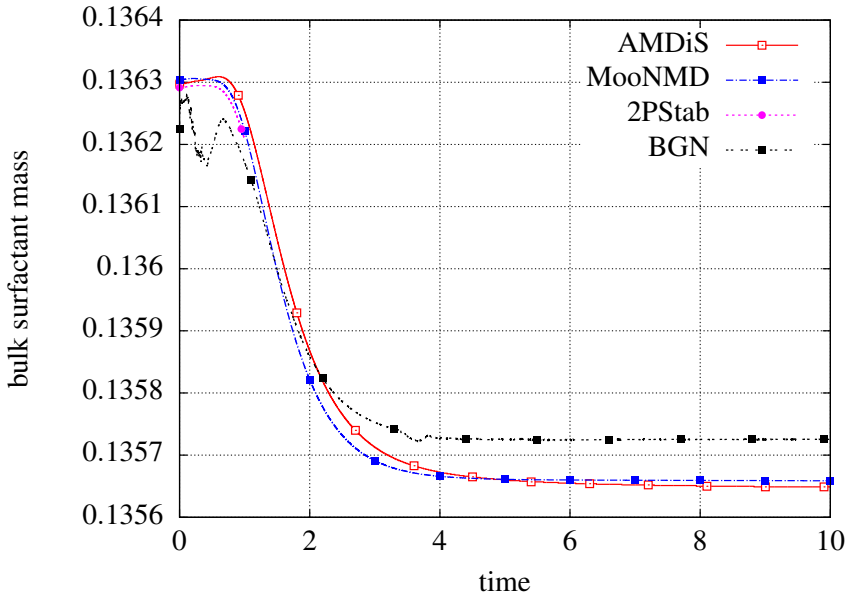

Fig. 3 Bulk surfactant mass over time, for $(c_0, Pe, Pe_\Gamma, E) = (0.02, 1, 1, 1)$.

lead to a slight, but steady, loss of surfactant mass over time. The deviation in the simulation using AMDiS at the beginning of the simulation cannot be explained, but in general the code shows the same overall behaviour as the other codes.

The stationary local distribution of surfactant in the bulk phase and on the surface is shown in Fig. 5, exemplarily for the stationary case with $(c_0, Pe, Pe_\Gamma, E) = (0.02, 1, 1, 1)$ (right) and $(c_0, Pe, Pe_\Gamma, E) = (0.02, 10, 10, 1)$ (left). The surface, the inner line, is scaled and translated a bit, in order to better distinguish it from the bulk. Note the different distribution due to different diffusion intensity. For both parameter regimes, surfactant is adsorbed at the bubble surface leading to a decrease in bulk surfactant next to the bubble. Along the bubble surface surfactant is transported with the flow to accumulate at the rear, where it is continuously desorbed to the bulk. In case of higher diffusion (left) local variations in surfactant concentration are more pronounced.

Fig. 6 displays the stationary bulk surfactant distribution along the channel wall for $(c_0, Pe, Pe_\Gamma, E) = (0.02, 1, 1, 1)$. We find excellent agreement among the numerical models and codes.

Finally, we investigate the effect of surfactant on the film thickness. Fig. 7 shows the film width over time for $(c_0, Pe, Pe_\Gamma, E) = (0.02, 1, 1, 0.5)$. The behavior of all four codes is similar and very close to each other. After some initial oscillations and interface waves, the bubble shape reaches a stationary state after a short time and the film width stays constant. The stationary film width is given for all codes and parameters in Tab. 4. All values are determined at $t = 10$, except for the code

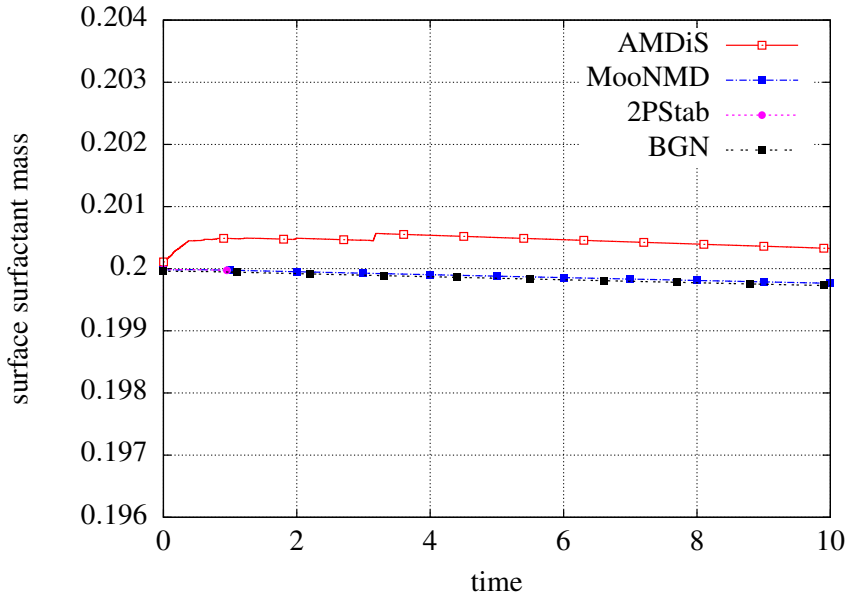

Fig. 4 Surface surfactant mass over time, for $(c_0, Pe, Pe_\Gamma, E) = (0.02, 1, 1, 1)$.

2PStab, for which they are taken at time $t = 1$, when the solution is already fairly stationary.

Table 4 Film width for different simulation parameters.

$c_0 = 0.02$	$Pe = Pe_\Gamma = 1$		$Pe = Pe_\Gamma = 10$	
	$E = 0.5$	$E = 1$	$E = 0.5$	$E = 1$
AMDiS	0.14408	0.14802	0.14304	0.14604
MooNMD	0.14724	0.15086	0.14601	0.14853
2PStab ($t = 1$)	0.14627	0.14957	0.14504	0.14739
BGN	0.14674	0.15053	0.14492	0.14789
$c_0 = 0.08$	$Pe = Pe_\Gamma = 1$		$Pe = Pe_\Gamma = 10$	
	$E = 0.5$	$E = 1$	$E = 0.5$	$E = 1$
AMDiS	0.14960	0.14914	-	-
MooNMD	0.15121	0.15113	0.15037	0.15032
2PStab ($t = 1$)	0.14962	-	-	-
BGN	0.15101	0.14932	0.14845	0.15144

In general the diffuse-interface models predict a smaller film thickness which might be due to a minimal Cahn–Hilliard dynamics that leads to a slight retraction of the bubble. This explanation is also supported by the slightly smaller bubble lengths of diffuse-interface models, seen in Tab. 5.

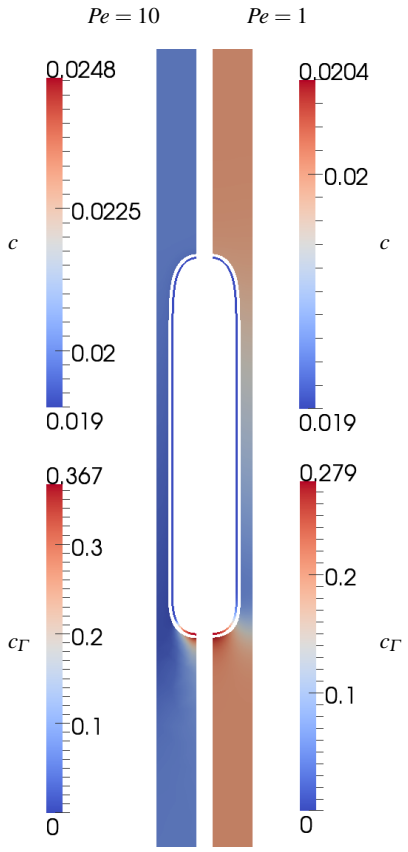

Fig. 5 Stationary surfactant distribution from MooNMD in the bulk phases and on the surface. For $(c_0, Pe, Pe_\Gamma, E = (0.02, 1, 1, 1)$ (right), and for $(c_0, Pe, Pe_\Gamma, E = (0.02, 10, 10, 1)$ (left). Note the different scalings.

Fig. 8 shows a comparison of the film width with varying surface elasticity E (left) and with varying diffusion coefficients Pe, Pe_Γ (right). All codes show that increasing surface elasticity and surfactant diffusibility leads to larger film thickness. This is consistent with analytical predictions conducted in [49]. Due to the chosen parameters, the change in film width across different parameters is minimal and the tiny differences between the codes may seem large. However, the differences in film thickness between the codes are smaller than 2% and the equal slope of the lines in Fig. 8 indicates good agreement between all four numerical codes with respect to changes in surfactant elasticity and diffusibility.

From Tab. 3 it can be seen that the bubble velocity is almost independent of the surfactant-related parameters, although the film thickness varies. This is in contrast to the results of [22] that predict an increasing bubble velocity with an increasing film width. This might be a unique behavior due to the presence of the surfactant that was not included in [22].

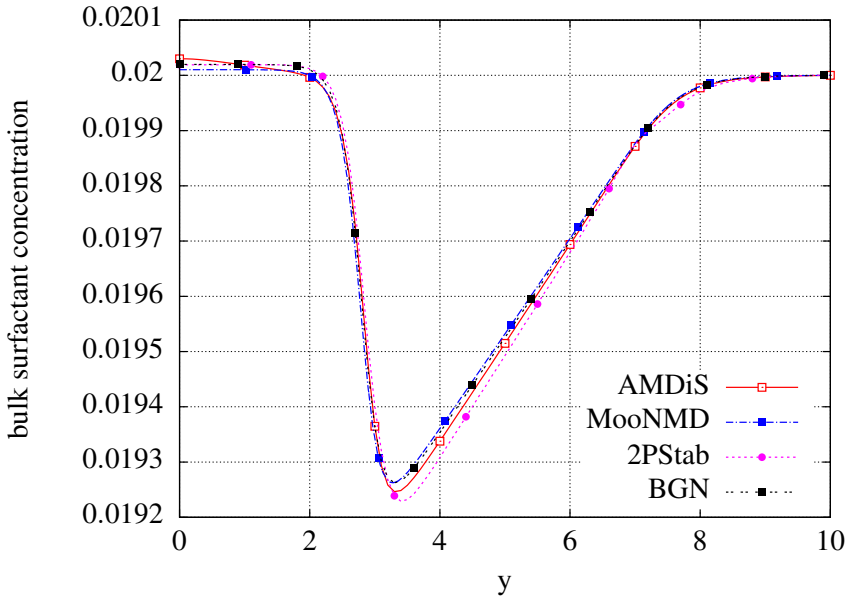

Fig. 6 Stationary bulk surfactant concentration along the channel wall at time $t = 10$ ($t = 1$ for 2PStab), for $(c_0, Pe, Pe_\Gamma, E) = (0.02, 1, 1, 1)$.

Table 5 Bubble length for different simulation parameters.

$c_0 = 0.02$	$Pe = Pe_\Gamma = 1$		$Pe = Pe_\Gamma = 10$	
	$E = 0.5$	$E = 1$	$E = 0.5$	$E = 1$
AMDiS	4.71900	4.72500	4.72000	4.73100
MooNMD	4.76351	4.77366	4.76632	4.77970
2PStab ($t = 1$)	4.73000	4.75000	4.74000	4.76000
BGN	4.75971	4.76951	4.76212	4.77465
$c_0 = 0.08$	$Pe = Pe_\Gamma = 1$		$Pe = Pe_\Gamma = 10$	
	$E = 0.5$	$E = 1$	$E = 0.5$	$E = 1$
AMDiS	4.76200	4.80000	-	-
MooNMD	4.81922	5.05115	4.87267	4.97512
2PStab ($t = 1$)	4.80000	-	-	-
BGN	4.81032	4.82561	4.81045	4.84463

5 Conclusion

We have presented a quantitative comparison of simulations based on diffuse- and sharp-interface models for two-phase flows with soluble surfactants. Therefore, we have extended the purely hydrodynamic benchmark study of Aland et al. [6] to a scenario with soluble surfactants. We considered a single Taylor bubble that assumes a stationary position in a channel flow as liquid inflow and buoyancy effects cancel

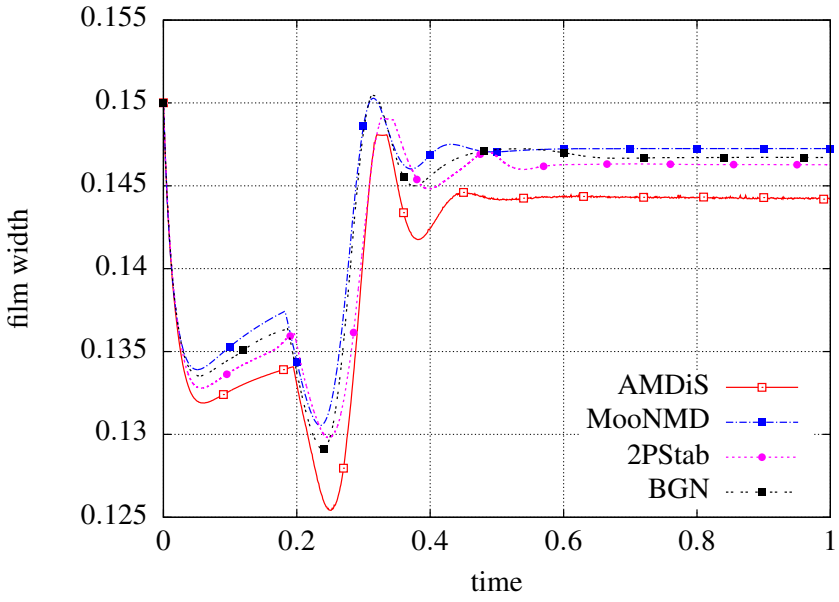

Fig. 7 Film width over time, for $(c_0, Pe, Pe_\Gamma, E) = (0.02, 1, 1, 0.5)$.

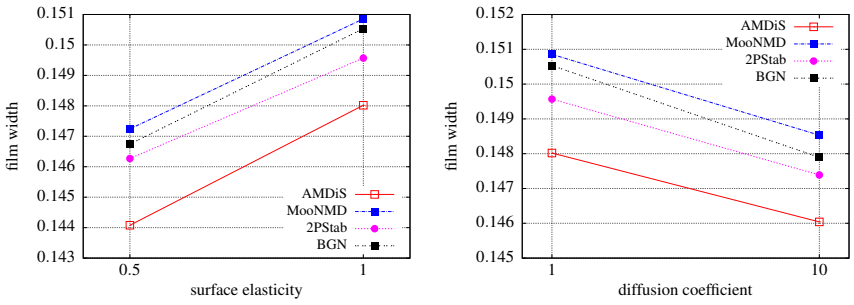

Fig. 8 Film width with surface elasticity for $(c_0, Pe, Pe_\Gamma) = (0.02, 1, 1)$ (left) and film width with diffusion coefficients for $(c_0, E) = (0.02, 1)$ (right).

each other out, which makes the scenario amenable to high resolution experimental imaging.

Several numerical simulations with different surfactant-related parameters were conducted with four numerical codes, two based on the diffuse-interface methods and two based on the sharp-interface methods. The codes were compared in terms of different benchmark quantities: the surfactant distribution, the film width between bubble and channel wall, the bubble length and the counter flow velocity required to keep the bubble stationary.

All four codes showed a quantitative agreement across all measured quantities. While bubble shapes and velocities were almost identical between the sharp-interface models, the diffuse-interface codes predicted a slightly smaller film thickness and bubble length which can be attributed to the Cahn–Hilliard dynamics leading to a minimal retraction of the bubble. The slight contraction of the bubble in the diffuse-interface models went along with an up to 3% smaller bubble velocity.

Furthermore, we analyzed the local distribution of surfactant in the system. Surfactant molecules are adsorbed at the bubble surface leading to a decrease in bulk surfactant next to the bubble. Along the bubble surface surfactant is transported with the flow to accumulate at the rear where it is then desorbed into the bulk. We found that all codes predicted almost identical values for the local surfactant distribution along the channel wall, in accordance with the characteristic decrease of the surfactant concentration in the film predicted in [49].

For increasing surfactant concentration and surface elasticity we found an increasing film thickness as predicted in [49]. Additionally, we observed an increase of the film width for higher surfactant diffusibility.

A further observation was that changes in the film width were not reflected in the counter flow velocity, which stayed nearly constant across all used parameters, contrary to the prediction of [22].

References

1. Abels, H., Garcke, H., Grün, G.: Thermodynamically consistent, frame indifferent diffuse interface models for incompressible two-phase flows with different densities. Math. Models Methods Appl. Sci. **22**(03), 1150,013 (2012)
2. Abels, H., Garcke, H., Lam, K.F., Weber, J.: Two-phase flow with surfactants: Diffuse interface models and their analysis. In: Advances in Mathematical Fluid Mechanics. Springer (2016). (a contribution in this book)
3. Ahmed, N., Matthies, G., Tobiska, L., Xie, H.: Discontinuous Galerkin time stepping with local projection stabilization for transient convection-diffusion-reaction problems. Comput. Methods Appl. Mech. Engrg. **200**(21–22), 1747–1756 (2011). DOI 10.1016/j.cma.2011.02.003
4. Aland, S.: Time integration for diffuse interface models for two-phase flow. J. Comput. Phys. **262**, 58–71 (2014)
5. Aland, S.: Phase field models for two-phase flow with surfactants and biomembranes. In: Advances in Mathematical Fluid Mechanics. Springer (2016). (a contribution in this book)
6. Aland, S., Boden, S., Hahn, A., Klingbeil, F., Weismann, M., Weller, S.: Quantitative comparison of Taylor flow simulations based on sharp-interface and diffuse-interface models. Int. J. Num. Meth. Fluids **73**, 344–361 (2013)
7. Aland, S., Egerer, S., Lowengrub, J., Voigt, A.: Diffuse interface models of locally inextensible vesicles in a viscous fluid. J. Comput. Phys. **277**, 32–47 (2014). URL http://dx.doi.org/10.1016/j.jcp.2014.08.016
8. Aland, S., Lehrenfeld, C., Marschall, H., Meyer, C., Weller, S.: Accuracy of two-phase flow simulations: The Taylor flow benchmark. Proc. Appl. Math. Mech. **13**(1), 595–598 (2013)
9. Aland, S., Lowengrub, J., Voigt, A.: A continuum model of colloid-stabilized interfaces. Phys. Fluids **23**(6), 062,103 (2011)
10. Aland, S., Voigt, A.: Benchmark computations of diffuse interface models for two-dimensional bubble dynamics. Int. J. Num. Meth. Fluids **69**(3), 747–761 (2011)

11. Angeli, P., Gavriilidis, A.: Hydrodynamics of Taylor flow in small channels: a review. Proc. IMechE Part C: J. Mech. Eng. Sci. **222**(5), 737–751 (2008)
12. Barrett, J.W., Garcke, H., Nürnberg, R.: On stable parametric finite element methods for the Stefan problem and the Mullins–Sekerka problem with applications to dendritic growth. J. Comput. Phys. **229**(18), 6270–6299 (2010). DOI 10.1016/j.jcp.2010.04.039. URL http://dx.doi.org/10.1016/j.jcp.2010.04.039
13. Barrett, J.W., Garcke, H., Nürnberg, R.: Numerical computations of faceted pattern formation in snow crystal growth. Phys. Rev. E **86**(1), 011,604 (2012). DOI 10.1103/PhysRevE.86.011604. URL http://dx.doi.org/10.1103/PhysRevE.86.011604
14. Barrett, J.W., Garcke, H., Nürnberg, R.: Eliminating spurious velocities with a stable approximation of viscous incompressible two-phase Stokes flow. Comput. Methods Appl. Mech. Engrg. **267**, 511–530 (2013). DOI 10.1016/j.cma.2013.09.023. URL http://dx.doi.org/10.1016/j.cma.2013.09.023
15. Barrett, J.W., Garcke, H., Nürnberg, R.: Numerical computations of the dynamics of fluidic membranes and vesicles. Phys. Rev. E **92**(5), 052,704 (2015). DOI 10.1103/PhysRevE.92.052704. URL http://dx.doi.org/10.1103/PhysRevE.92.052704
16. Barrett, J.W., Garcke, H., Nürnberg, R.: On the stable numerical approximation of two-phase flow with insoluble surfactant. M2AN Math. Model. Numer. Anal. **49**(2), 421–458 (2015). DOI 10.1051/m2an/2014039. URL http://dx.doi.org/10.1051/m2an/2014039
17. Barrett, J.W., Garcke, H., Nürnberg, R.: Stable finite element approximations of two-phase flow with soluble surfactant. J. Comput. Phys. **297**, 530–564 (2015). DOI 10.1016/j.jcp.2015.05.029. URL http://dx.doi.org/10.1016/j.jcp.2015.05.029
18. Barrett, J.W., Garcke, H., Nürnberg, R.: Stable numerical approximation of two-phase flow with a Boussinesq–Scriven surface fluid. Commun. Math. Sci. **13**(7), 1829–1874 (2015). DOI 10.4310/CMS.2015.v13.n7.a9. URL http://dx.doi.org/10.4310/CMS.2015.v13.n7.a9
19. Barrett, J.W., Garcke, H., Nürnberg, R.: A stable parametric finite element discretization of two-phase Navier–Stokes flow. J. Sci. Comp. **63**(1), 78–117 (2015). DOI 10.1007/s10915-014-9885-2. URL http://dx.doi.org/10.1007/s10915-014-9885-2
20. Barrett, J.W., Garcke, H., Nürnberg, R.: A stable numerical method for the dynamics of fluidic biomembranes. Numer. Math. **134**(4), 783–822 (2016). DOI 10.1007/s00211-015-0787-5. URL http://dx.doi.org/10.1007/s00211-015-0787-5
21. Boden, S., dos Santos Rolo, T., Baumbach, T., Hampel, U.: Synchrotron radiation microtomography of Taylor bubbles in capillary two-phase flow. Exp. Fluids **55**(7), 1768 (2014). DOI 10.1007/s00348-014-1768-7. URL http://dx.doi.org/10.1007/s00348-014-1768-7
22. Bretherton, F.: The motion of long bubbles in tubes. J. Fluid. Mech. **10**(02), 166–188 (1961)
23. Ganesan, S., Hahn, A., Held, K., Tobiska, L.: An accurate numerical method for computation of two-phase flows with surfactants. In: European Congress on Computational Methods in Applied Sciences and Engineering (ECCOMAS 2012), J. Eberhardsteiner et. al.(eds.), Vienna, Austria, September, pp. 10–14 (2012)
24. Ganesan, S., Hahn, A., Simon, K., Tobiska, L.: Finite element computations for dynamic liquid–fluid interfaces. In: Computational Methods for Complex Liquid-Fluid Interfaces. CRC Press (2015)
25. Ganesan, S., Tobiska, L.: A coupled arbitrary Lagrangian–Eulerian and Lagrangian method for computation of free surface flows with insoluble surfactants. J. Comput. Phys. **228**(8), 2859 – 2873 (2009). DOI 10.1016/j.jcp.2008.12.035
26. Ganesan, S., Tobiska, L.: Arbitrary Lagrangian–Eulerian finite-element method for computation of two-phase flows with soluble surfactants. J. Comput. Phys. **231**(9), 3685 – 3702 (2012). DOI 10.1016/j.jcp.2012.01.018
27. Ganesan, S., Tobiska, L.: An operator-splitting finite element method for the efficient parallel solution of multi-dimensional population balance systems. Chem. Eng. Sci. **69**, 59–68 (2012)
28. Garcke, H., Hinze, M., Kahle, C.: A stable and linear time discretization for a thermodynamically consistent model for two-phase incompressible flow. Appl. Numer. Math. **99**, 151–171 (2016)
29. Garcke, H., Lam, K., Stinner, B.: Diffuse interface modelling of soluble surfactants in two-phase flow. Comm. Math. Sci. **12**(8), 1475–1522 (2014)

30. Gollwitzer, C., Matthies, G., Richter, R., Rehberg, I., Tobiska, L.: The surface topography of a magnetic fluid – a quantitative comparison between experiment and numerical simulation. J. Fluid Mech. **571**, 455–474 (2007)
31. Günther, A., Jhunjhunwala, M., Thalmann, M., Schmidt, M.A., Jensen, K.F.: Micromixing of miscible liquids in segmented gas-liquid flow. Langmuir **21**(4), 1547–1555 (2005). DOI 10.1021/la0482406
32. Halpern, D., Gaver, D.: Boundary element analysis of the time-dependent motion of a semi-infinite bubble in a channel. J. Comput. Phys. **115**(2), 366–375 (1994)
33. Hayashi, K., Tomiyama, A.: Effects of surfactant on terminal velocity of a Taylor bubble in a vertical pipe. Int. J. Multiph. Flow **39**, 78–87 (2012)
34. Hysing, S., Turek, S., Kuzmin, D., Parolini, N., Burman, E., Ganesan, S., Tobiska, L.: Quantitative benchmark computations of two-dimensional bubble dynamics. Internat. J. Numer. Methods Fluids **60**(11), 1259–1288 (2009). DOI 10.1002/fld.1934
35. Iliescu, T., John, V., Layton, W.J., Matthies, G., Tobiska, L.: A numerical study of a class of LES models. Int. J. Comput. Fluid Dyn. **17**(1), 75–85 (2003). DOI 10.1080/1061856021000009209
36. John, V.: Higher order finite element methods and multigrid solvers in a benchmark problem for the 3D Navier–Stokes equations. Internat. J. Numer. Methods Fluids **40**(6), 775–798 (2002). DOI 10.1002/fld.377
37. John, V.: Reference values for drag and lift of a two-dimensional time-dependent flow around a cylinder. Internat. J. Numer. Methods Fluids **44**(7), 777–788 (2004). DOI 10.1002/fld.679
38. John, V., Matthies, G.: Higher-order finite element discretizations in a benchmark problem for incompressible flows. Internat. J. Numer. Methods Fluids **37**(8), 885–903 (2001). DOI 10.1002/fld.195
39. John, V., Matthies, G.: MooNMD – a program package based on mapped finite element methods. Comput. Vis. Sci. **6**, 163–170 (2004). DOI 10.1007/s00791-003-0120-1
40. John, V., Mitkova, T., Roland, M., Sundmacher, K., Tobiska, L., Voigt, A.: Simulations of population balance systems with one internal coordinate using finite element methods. Chem. Eng. Sci. **64**(4), 733 – 741 (2009). DOI 10.1016/j.ces.2008.05.004. 3rd International Conference on Population Balance Modelling
41. Krasnyk, M., Mangold, M., Ganesan, S., Tobiska, L.: Numerical reduction of a crystallizer model with internal and external coordinates by proper orthogonal decomposition. Chem. Eng. Sci. **70**(0), 77 – 86 (2012). DOI 10.1016/j.ces.2011.05.053. 4th International Conference on Population Balance Modeling
42. Kreutzer, M.T., Kapteijn, F., Moulijn, J.A., Heiszwolf, J.J.: Multiphase monolith reactors: Chemical reaction engineering of segmented flow in microchannels. Chem. Eng. Sci. **60**(22), 5895–5916 (2005). DOI 10.1016/j.ces.2005.03.022
43. Lavrova, O., Matthies, G., Mitkova, T., Polevikov, V., Tobiska, L.: Finite element methods for coupled problems in ferrohydrodynamics. In: Challenges in Scientific Computing - CISC 2002, *Lecture Notes in Computational Science and Engineering*, vol. 35, pp. 160–183. Springer Berlin Heidelberg (2003)
44. Lowengrub, J., Allard, J., Aland, S.: Numerical simulation of endocytosis: Viscous flow driven by membranes with non-uniformly distributed curvature-inducing molecules. J. Comput. Phys. **309**, 112–128 (2016). DOI 10.1016/j.jcp.2015.12.055. URL https://dx.doi.org/10.1016/j.jcp.2015.12.055
45. Marschall, H., Boden, S., Lehrenfeld, C., Falconi Delgado, C., Hampel, U., Reusken, A., Wörner, M., Bothe, D.: Validation of interface capturing and tracking techniques with different surface tension treatments against a Taylor bubble benchmark problem. Comput. & Fluids **102**, 336–352 (2014)
46. Matthies, G., Tobiska, L.: A two-level local projection stabilisation on uniformly refined triangular meshes. Numer. Algorithms **61**, 465–478 (2012). DOI 10.1007/s11075-012-9543-4
47. Muradoglu, M., Günther, A., Stone, H.A.: A computational study of axial dispersion in segmented gas-liquid flow. Phys. Fluids **19**(7) (2007). DOI 10.1063/1.2750295
48. Olgac, U., Muradoglu, M.: Effects of surfactant on liquid film thickness in the Bretherton problem. Int. J. Multiph. Flow **48**, 58–70 (2013)

49. Ratulowski, J., Chang, H.C.: Marangoni effects of trace impurities on the motion of long gas bubbles in capillaries. J. Fluid Mech. **210**, 303–328 (1990)
50. Roy, S., Bauer, T., Al-Dahhan, M., Lehner, P., Turek, T.: Monoliths as multiphase reactors: A review. AIChE J. **50**(11), 2918–2938 (2004). DOI 10.1002/aic.10268
51. Schmidt, A., Siebert, K.G.: Design of Adaptive Finite Element Software: The Finite Element Toolbox ALBERTA, *Lecture Notes in Computational Science and Engineering*, vol. 42. Springer-Verlag, Berlin (2005)
52. Williams, J.L.: Monolith structures, materials, properties and uses. Catal. Today **69**(1–4) (2001). DOI 10.1016/S0920-5861(01)00348-0